Electronic structure and hyperfine interactions of T, T* and T' phases of $(La_{1-x}Gd_x)_2Cu_{1-y}Fe_yO_4$

1995 J. Phys.: Condens. Matter 7 5025

(http://iopscience.iop.org/0953-8984/7/26/008)

J. Phys.: Condens. Matter 7 (1995) 5025–5043. Printed in the UK

Electronic structure and hyperfine interactions of T, T* and T′ phases of $(La_{1-x}Gd_x)_2Cu_{1-y}Fe_yO_4$

Liqun Guo†, D E Ellis† and E Baggio-Saitovitch‡

† Department of Physics, Northwestern University, Evanston, IL 60208, USA

‡ Centro Brasileiro de Pesquisas Fisicas, Rio de Janeiro, Brazil

Received 13 February 1995, in final form 4 April 1995

Abstract. Electronic structures and hyperfine interactions associated with the Cu–O environment of T, T*, and T′ phases of $(La_{1-x}Gd_x)_2CuO_4$ were studied, using the density functional theory in an embedded cluster approach. Mössbauer isomer shifts, electric field gradients and contact hyperfine fields for Fe-substituted species were determined for comparison with experiments performed on $Fe:(La, Gd)_{1.85}Sr_{0.15}CuO_4$. These data are used to describe the response of charge and spin densities around Cu sites to sixfold (T), fivefold (T*), and fourfold (T′) oxygen coordination.

1. Introduction

An extraordinary amount of attention has recently been focused on $(La_{1-x}Gd_x)_2Cu_{1-y}Fe_yO_4$ copper-oxide-based ceramics [1–3]. Theoretical and experimental studies of the electronic structure have been carried out in the quest for the mechanisms responsible for high-temperature superconductivity, and to characterize materials for electronic and sensor materials applications. Many hyperfine interaction (HFI) experiments and theoretical works have been reported on materials doped with impurities, often connected with studies of variation of T_c and changes of oxygen stoichiometry [4–7].

Among the isovalent rare earth substituents, the Gd compounds $(La_{1-x}Gd_x)_2CuO_4$ provide an excellent 'test set' in which the structure is both variable and yet very well defined. In this system, there exist three stable phases (T, T* and T′), in which the local Cu–O unit is octahedral (sixfold), pyramidal (fivefold), and square (fourfold), respectively. [8] In this paper we consider all three cases with composition: T phase (La_2CuO_4), T* phase ($(La_{1-x}Gd_x)_2CuO_4$) ($0.42 \leqslant x \leqslant 0.49$) and T′ phase ($Gd_2CuO_4$). The self-consistent electronic structure, with resulting energy levels, charge and spin densities, and densities of states (DOS) are studied. In addition, ^{57}Fe substitution for Cu in these compounds is calculated and compared with the experimental data.

^{57}Fe is expected to substitute for Cu because of its known chemical similarity and size. Through Mössbauer spectroscopy, it is a very useful probe for revealing local magnetic fields, charge densities, and electric field gradients. However, Fe is not a totally 'innocent' bystander in determining the local environment, due to its affinity for oxygen. In view of neutron and x-ray studies on related materials, it is clear that the local environment of the Fe site in Fe-doped La_2CuO_4, $(La_{1-x}Gd_x)_2CuO_4$ and Gd_2CuO_4 can be quite complicated. From the microstructural view, the x-ray absorption and Mössbauer studies of $^{57}Fe:YBa_2Cu_3O_7$ allowed us to establish a preferential occupation of the Cu(1) site which may have several different local oxygen and Fe-clustered configurations [9–13].

0953-8984/95/265025+19$19.50

In the present work, the electric field gradient (EFG), isomer shift, and magnetic hyperfine field are determined for ^{57}Fe in plausible geometries. A comparison is made with experiments in order to find the common and different properties among T, T*, and T′ phases. A primary goal is to establish the relationships between local coordination to oxygen and bonding and hyperfine properties.

2. Theoretical model

2.1. Local density discrete variational method

In this work all calculations were performed using the self-consistent first-principles density functional theory. Single-particle orbitals are obtained using the discrete variational (DV X_α) method [14–17]. The Hamiltonian consists of the sum of a kinetic energy operator, nuclear and electronic Coulomb potentials, and an exchange and correlation potential. Eigenfunctions of the effective Hamiltonian are expanded in a basis of numerical atomic orbitals, and the potential is iterated to self-consistency.

Numerical free-atom basis functions $\{A_j\}$ were used to obtain the molecular eigenfunctions as a linear combination of atomic orbitals (LCAO),

$$\Psi_i(r) = \sum_j A_j(r)\ C_{ij}. \tag{1}$$

The Mulliken atomic orbital populations and related partial densities of states can be used to develop a detailed chemically appealing description of the local atomic environment.

2.2. Charge and spin density

In the non-relativistic approach, the density of electrons of spin components $s_z = \sigma$ is

$$\rho_\sigma(r) = \sum_i f_{i\sigma}\,|\Psi_{i\sigma}(r)|^2 \tag{2}$$

where $f_{i\sigma}$ are the occupation numbers which are chosen for the ground state according to Fermi–Dirac statistics, and Ψ_i are the single-particle orbitals which are self-consistently generated. The charge and spin densities are $\rho_c = \rho^+ + \rho_-$ and $\rho_s = \rho^+ - \rho_-$, respectively, and can in principle be measured by x-ray and neutron diffraction on single-crystal specimens.

2.3. Embedding schemes

Cluster models are used to describe the local environment of a fragment of an extended solid. Many spectroscopic and physical–chemical properties are controlled by near-neighbour interactions, so clusters of modest size can be employed. Embedding schemes form part of the strategy of setting up boundary conditions and potentials which reflect the interaction of the cluster atoms and their electrons with the external 'host' [18–19].

2.4. Density of states

The energy spectrum of valence eigenfunctions is best displayed as an energy- dependent density of states. The contribution of state nl of atom ν to the DOS is represented by

$$D^\nu_{nl}(E) = \sum_p f^\nu_{nl,p} L(E - \varepsilon_p,\ \sigma) \tag{3}$$

where $f_{nl,p}$ is the appropriate Mulliken population [20] contribution to the pth molecular orbital. $L(E-\varepsilon_p, \sigma)$ is a line shape function chosen as a Lorentzian of width σ. By summing all partial DOSs, we obtain the total DOS

$$D(E) = \sum_{vnl} D_{nl}^{v} = \sum_{p} L(E-\varepsilon_p, \sigma). \tag{4}$$

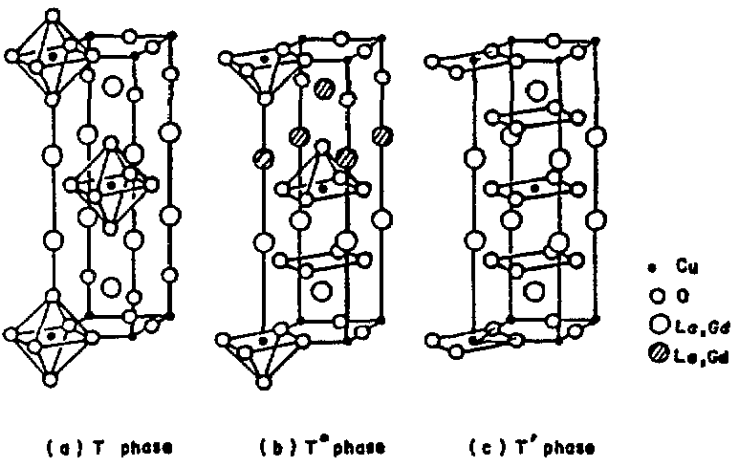

Figure 1. Crystal structures for T, T*, and T' phases in the $(La_{1-x}Gd_x)_2CuO_4$ system.

2.5. *Mössbauer isomer shift (IS)*

The ^{57}Fe IS of the Mössbauer spectra (nuclear gamma resonance, NGR) reflects the monopole interaction of the nuclear charge volume and the overlapping electronic charge density. It can be written as

$$\text{IS} = A_{\text{IS}}\, \Delta\rho_c(0) \tag{5}$$

where A_{IS} depends upon nuclear ground and excited state radial distributions, and $\Delta\rho_c(0)$ is the difference in electron density at the nucleus for the host crystal and a reference system such as metallic iron [21]. Presently accepted values of A_{IS} lie in the range -0.25 ± 0.05 mm a_0^3 s^{-1}.

2.6. *Electric field gradient (EFG)*

Transitions between the $I = \frac{3}{2}$ excited state and the $I = \frac{1}{2}$ nuclear ground state of ^{57}Fe lead to quadrupolar splitting (QS) proportional to the EFG. A convenient form is given by

$$\text{QS} = BQV_{zz}\left(1+\frac{\eta^2}{3}\right)^{1/2} \tag{6}$$

where $B = 11.77$ mm a_0^3 b^{-1} s^{-1} $= 200.1$ MHz a_0^3 b^{-1} (b = barn) and Q is the nuclear quadrupole moment. Suggested values of Q range between 0.08 and 0.21 b [22]. The eigenvalues of the field gradient tensor V_{ij} are labelled in order of increasing absolute value as V_{xx}, V_{yy}, V_{zz}. The experimentally determined quantities are the principal value V_{zz} and the asymmetry parameter,

$$\eta = \left|(V_{yy}-V_{xx})/V_{zz}\right|. \tag{7}$$

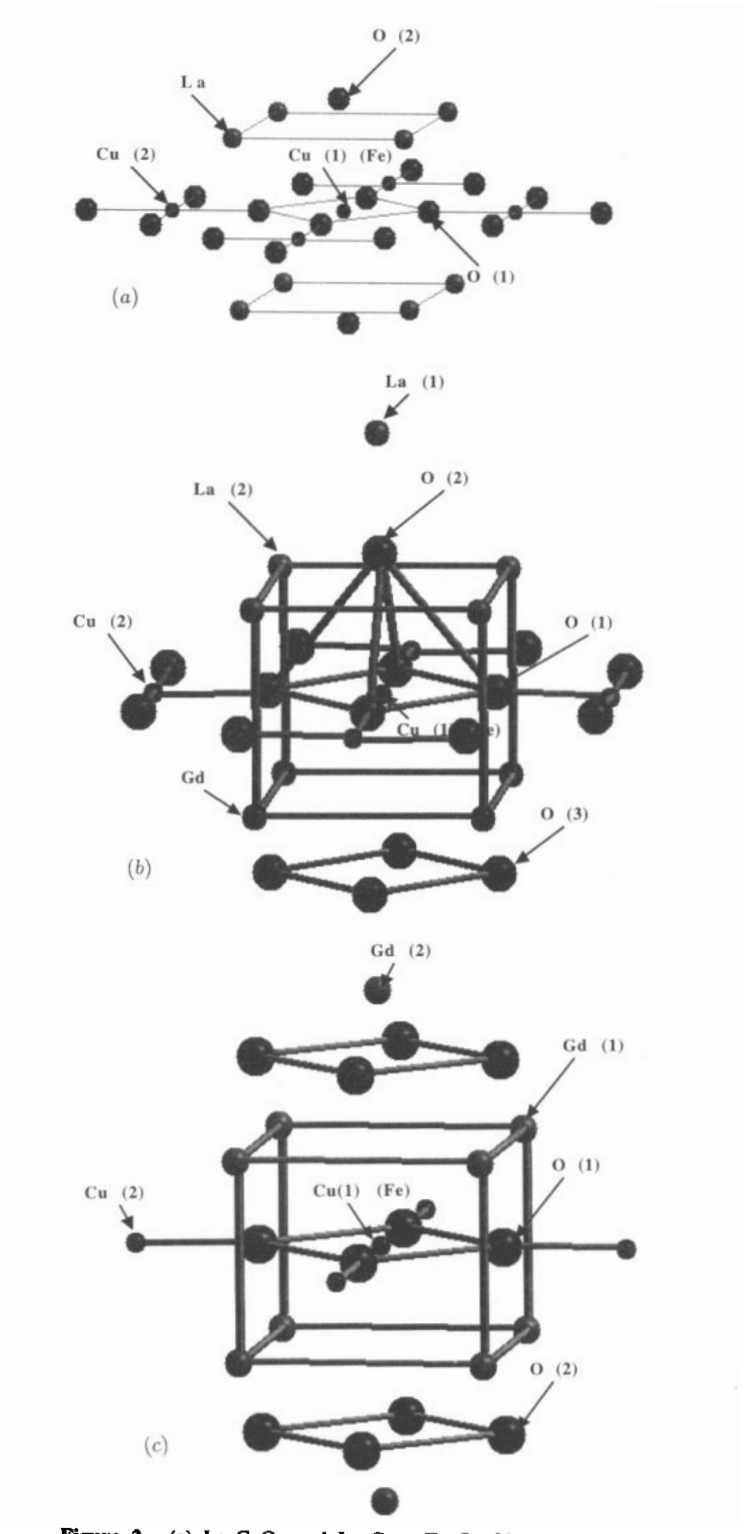

Figure 2. (a) La_2CuO_4 and $La_2Cu_{1-y}Fe_yO_4$ 31-atom cluster; (b) $(La_{1-x}Gd_x)_2CuO_4$ and $(La_{1-x}Gd_x)_2Cu_{1-y}Fe_yO$ 31-atom cluster; (c) Gd_2CuO_4 and $Gd_2Cu_{1-y}Fe_yO_4$ 27-atom cluster.

The total EFG required to determine the quadrupolar splitting is found by combining the valence electron matrix element with contributions of the exterior crystal ions, core electrons, and nuclei of the local cluster with the appropriate sign. For example,

$$V_{zz}(\text{total}) = \sum_{\nu}^{\text{cluster}} Q_\nu^c(3z_\nu^2 - r_\nu^2)/r^5 - \langle \rho_c(3z^2 - r^2)/r^5 \rangle + \sum_{\nu}^{\text{exterior}} q_\nu(3z_\nu^2 - r_\nu^2)/r_\nu^5 \tag{8}$$

where $Q_\nu^c = Z_\nu - N_\nu^c$ is the charge of the ionic core for the ion at site ν, q_ν are net ionic charges.

2.7. Magnetic hyperfine field

Interaction of the nuclear magnetic moment with spin magnetism of electrons at the nucleus leads to an energy

$$E_s = -g_N \mu_N H_s(0) \tag{9}$$

where the Fermi contact field $H_s(0) = A_s \rho_s(0)$ and $A_s = 52.42$ T a_0^3.

3. Results

3.1. Embedded cluster models

There exist three stable phases T, T*, and T′ of the $(La_{1-x}Gd_x)_2CuO_4$ system. Pure La_2CuO_4 is found in the T phase, which is shown in figure 1(a); the local Cu–O unit is a distorted octahedron (sixfold coordination of oxygen to Cu). $(La_{1-x}Gd_x)_2CuO_4$ has a T* phase in the range $0.42 \leqslant x \leqslant 0.49$, which is shown in figure 1(b), and the local Cu–O unit is a pyramid (fivefold). Gd_2CuO_4 adopts the T′ phase, which is shown in figure 1(c); here the local Cu–O unit is a square (fourfold).

For La_2CuO_4 and $La_2Cu_{1-y}Fe_yO_4$, we choose 31-atom embedded clusters M–O(4)–O(2)–La(8)–Cu(4)–O(12) (M = Cu or Fe), shown in figure 2(a). For $(La_{1-x}Gd_x)_2CuO_4$ and $(La_{1-x}Gd_x)_2Cu_{1-y}Fe_yO_4$, we choose 31-atom clusters M–O(5)–La(5)–Gd(4)–O(4)–Cu(4)–O(8) shown in figure 2(b), with the substituted Fe on the Cu(1) site. For Gd_2CuO_4 and $Gd_2Cu_{1-y}Fe_yO_4$, we choose 27-atom clusters M–O(4)–Gd(8)–O(8)–Cu(4)–Gd(2) shown in figure 2(c). Here too, the substituted Fe atom is on the Cu(1) site. In every case, Coulomb and exchange–correlation potential contributions of the infinite host crystal are included in the one-electron Hamiltonian.

3.2. Electronic structures

3.2.1. T phase. Self-consistent-field DV X_α calculations for La_2CuO_4 have been previously reported [6, 7]. As shown in table 1, the effective ionic configuration of Cu was found to be $Cu^{1.83+}3d^{9.06}4s^{0.07}4p^{0.03}$; i.e., the nominal $Cu^{2+}d^9s^0$ configuration is augmented by covalent charge sharing with oxygen ligands. The La ions are quite close to the 'ideal' 3+ state, with only $0.1e$ additionally involved in La–O bonding.

Experimentally, low-temperature antiferromagnetic order is found with variously reported moments of 0.4 [23], 0.5 [24], and 1.1 [25] μ_B per copper ion, in general markedly less than the Cu^{2+} spin-only free ion value of 1.73 μ_B. The present theoretical results predict rather small antiferromagnetically coupled moments at Cu sites in the perfect La_2CuO_4 crystal, perhaps due to the small cluster size and its symmetry restrictions. Spin on the copper ion at the centre is calculated to be only -0.02 μ_B, increasing in magnitude a little at the periphery to $+0.03$ μ_B.

Table 1. Charge and spin atomic orbital populations for T phase M–O(4)–O(2)–La(8)–Cu(4)–O(12) clusters.

		M = copper		M = iron	
		Charge	Spin	Charge	Spin
M[a]	3d	9.06	−0.016	5.85	4.017
	4s	0.07	0.000	0.05	0.078
	4p	0.03	0.000	0.03	−0.033
Total		1.83	−0.016	2.06	4.128
O[b]	2s	1.99	0.000	1.98	−0.001
	2p	5.84	0.001	5.82	0.041
Total		−1.83	0.001	−1.80	0.040
O[c]	2s	2.00	0.000	2.00	−0.001
	2p	5.94	−0.000	5.92	0.010
Total		−1.93	0.000	−1.91	0.009
La[d]	5p	5.99	0.000	5.99	0.001
	5d	0.09	−0.000	0.12	0.003
	6s	0.02	−0.000	0.02	0.001
Total		2.90	−0.000	2.88	−0.002
Cu[e]	3d	9.01	0.035	9.05	0.092
	4s	0.15	−0.001	0.15	−0.003
	4p	0.04	−0.000	0.05	0.002
Total		1.81	0.035	1.75	0.091
O[f]	2s	1.99	0.000	1.99	0.000
	2p	5.94	0.001	5.94	0.003
Total		−1.93	0.001	−1.93	0.003
O[g]	2s	1.99	0.000	1.99	0.001
	2p	5.93	0.001	5.92	0.005
Total		−1.92	0.001	−1.91	0.006

[a] Cu(1) or Fe on the centre of the centre plane.
[b] O(1) on four (a, b) centre plane sites.
[c] O(2) on axial sites.
[d] La on (a, b) plane sites.
[e] Cu(2) on centre plane sites.
[f] O(3) and O(4) around Cu(2) atoms.
[g] O(4) around Cu(2) atoms.

Fe impurity calculations were carried out on the Fe-centred 31-atom cluster embedded in the previously obtained La_2CuO_4 self-consistent lattice. A calculated configuration of $Fe^{2.06+}$ $3d^{5.85}$ $4s^{0.05}$ $4p^{0.03}$ with the maximal spin of 4.1 μ_B agrees with experimental values of 3–5 μ_B [26]. Perturbations on surrounding neighbours charge and spin densities are small, but perceptible. All six oxygen neighbours lose 0.02–0.03e, and their spin polarization moment gains about 0.01–0.04 μ_B compared to the Cu–centred case. The spin coupling to the next-nearest-neighbour Cu(2) sites leads to a small increase in Cu moment to 0.09 μ_B, antiferromagnetically coupled to Fe.

Direct valence density maps are rather uninteresting, showing mostly ionic bonding character, with some evidence of oxygen polarization and M–O shared charge. Valence charge density difference contour maps of $La_2Cu_{1-y}Fe_yO_4$ and La_2CuO_4 on a (100) plane and (110) plane are shown in figure 3(a) and 3(b), respectively. These figures emphasize the changes in electronic structure which occur due to metal substitution. No lattice relaxation effects were included, so as to make point by point comparisons possible. On the (100)

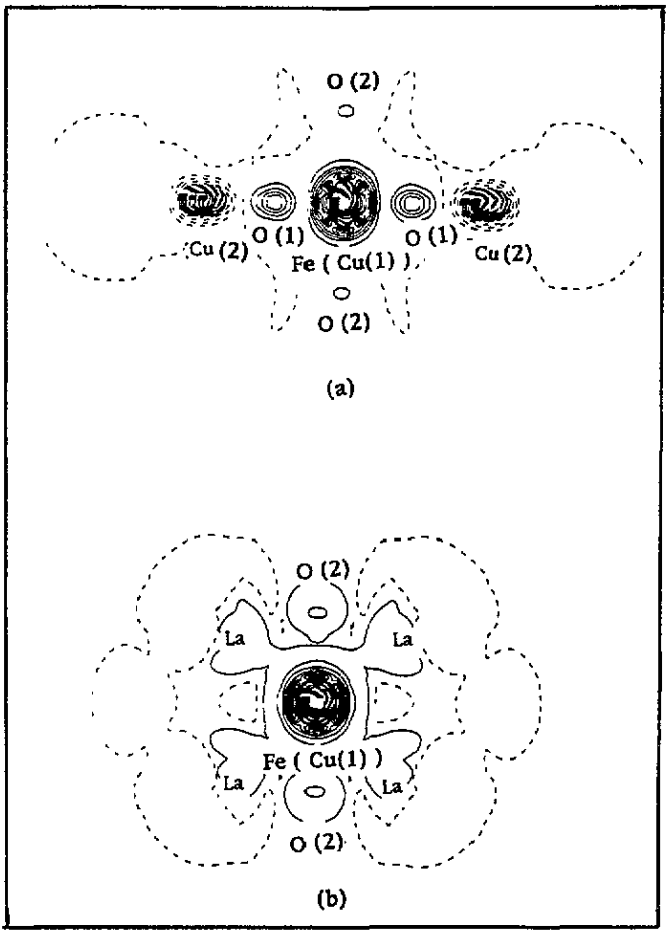

Figure 3. - - - Valence charge density difference contour map of T phase: $\rho[La_2Cu_{1-y}Fe_yO_4] - \rho[La_2CuO_4]$ on (a) (100) plane containing four equatorial oxygen, $-2.55 < \rho < 0.12e/a_0^3$; (b) (110) plane containing two axial oxygen, $-2.50 < \rho < 0.10e/a_0^3$. Contour interval is $0.01e/a_0^3$; dotted lines are negative values.

plane, we can see that the charge densities are increased on the four equatorial oxygen atoms after substituting Fe in the centre site. The charge densities on the next nearest Cu(2) sites are decreased. The bond length between the four equatorial oxygens and the centre site is about 1.89 Å, while the bond length between the two axial site oxygens and the centre site is about 2.42 Å. On the (110) plane, after substituting, the axial oxygen charge increases slightly and the weak bond charge between the four (a, b) plane La and the centre metal site is also increased.

The partial densities of states (PDOSs) for La_2CuO_4 Cu(1) 3d, 4sp, O(1) and O(2) 2sp are shown in figure 4(a); those for $La_2Cu_{1-y}Fe_yCuO_4$ Fe 3d, 4sp, Cu(2) 3d, 4sp and O(1) and O(2) 2sp are shown in figure 5(a). In these graphs, we choose the Fermi energy (E_F) of the cluster as the zero point of the energy axis. The Fe 3d PDOS has two major peaks about 1–5 eV below the Fermi energy which can be associated with crystal field splitting of the $d^5\uparrow$ complex of levels. The rather large exchange splitting leads to a similar $d^5\downarrow$ complex above E_F. In addition to 'crystal field' and exchange splitting effects in the Fe

Table 2. Charge and spin atomic orbital populations for T* phase M–O(5)–La(5)–Gd(4)–O(4)–Cu(4)–O(8) clusters.

		M = copper		M = iron	
		Charge	Spin	Charge	Spin
M[a]	3d	9.15	−0.001	5.62	3.905
	4g	0.07	0.000	0.24	0.019
	4p	0.02	−0.000	0.21	−0.001
Total		1.75	−0.001	1.93	3.919
O[b]	2s	1.98	−0.000	1.98	−0.002
	2p	5.77	0.004	5.78	0.025
Total		−1.75	0.004	1.76	0.023
O[c]	2s	1.99	−0.000	1.98	−0.002
	2p	5.84	0.000	5.86	0.019
Total		−1.83	0.003	−1.84	0.017
La[d]	5p	5.95	0.000	5.91	0.002
	5d	0.17	0.000	0.17	0.004
	6s	0.02	0.000	0.03	0.000
Total		2.87	0.000	2.88	0.006
Gd[e]	4f	7.10	6.886	7.12	6.871
	5p	5.98	0.003	5.98	0.002
	5d	0.11	0.023	0.11	0.024
	6s	0.03	−0.000	0.03	−0.001
Total		2.77	6.911	2.76	6.896
La[f]	5p	5.99	0.000	5.99	0.001
	5d	0.08	−0.000	0.07	0.001
	6s	0.02	−0.000	0.02	0.002
Total		2.92	0.000	2.91	0.005
O[g]	2s	2.00	0.000	2.00	0.000
	2p	5.85	0.047	5.86	0.037
Total		−1.85	0.047	−1.86	0.037
Cu[h]	3d	9.09	0.033	9.07	−0.577
	4s	0.15	0.001	0.17	−0.020
	4p	0.04	0.000	0.05	−0.008
Total		1.73	0.034	1.70	−0.606

[a] Cu(1) or Fe at the centre.
[b] O(1) on four (a, b) centre plane sites.
[c] O(2) on top axial site.
[d] La(1) on top axial site.
[e] Gd on four (a, b) plane sites.
[f] La(2) on four (a, b) plane sites.
[g] O(3) on four lower (a, b) plane sites.
[h] Cu(2) on centre plane sites.

3d PDOS, we can clearly see strong Fe d/O p covalent bonding structure extending to the bottom of the valence band, ~9 eV below E_F. The Cu 3d PDOS has only one large peak, centred about 2 eV below E_F. While the spin-dependent exchange splitting is quite small, we can see evidence of Cu d/O p covalency in structure near the bottom of the valence band, as seen with Fe. The weak Cu or Fe 4sp character is spread across the entire valence band as expected for very diffuse states. The main features of the PDOS obtained in cluster calculations are seen to be rather similar to those found in periodic band structure studies. The PDOSs of O 2s, 2p states which dominate the region down to $E_F - 20$ eV are quite

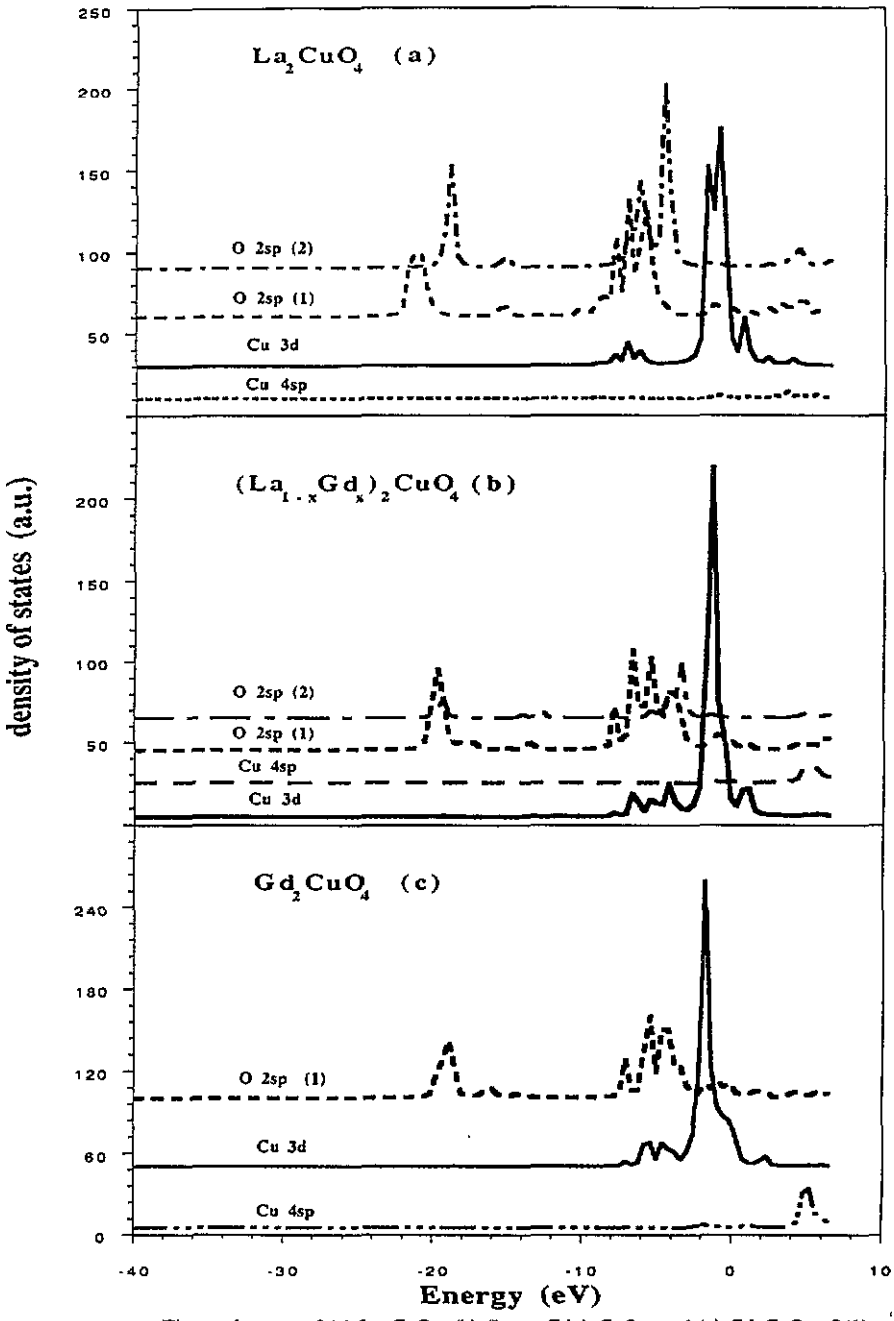

Figure 4. PDOS of (a) La_2CuO_4, (b) $(La_{1-x}Gd_x)_2CuO_4$, and (c) Gd_2CuO_4. O(1) are equatorial oxygen; O(2) are in axial or apical positions. Curves are offset vertically for energy viewing

similar, for either Cu- or Fe-centred clusters. In the centre plane, the O 2s character is mostly concentrated ~20 eV below E_F, and 2p states form the valence band extending to ~10 eV below the Fermi energy. There is a predicted relative shift of about 2 eV for the PDOS of the axial O(2) relative to equatorial O(1) ions in the T phase, with O(2) being less bound, due to the larger bond length.

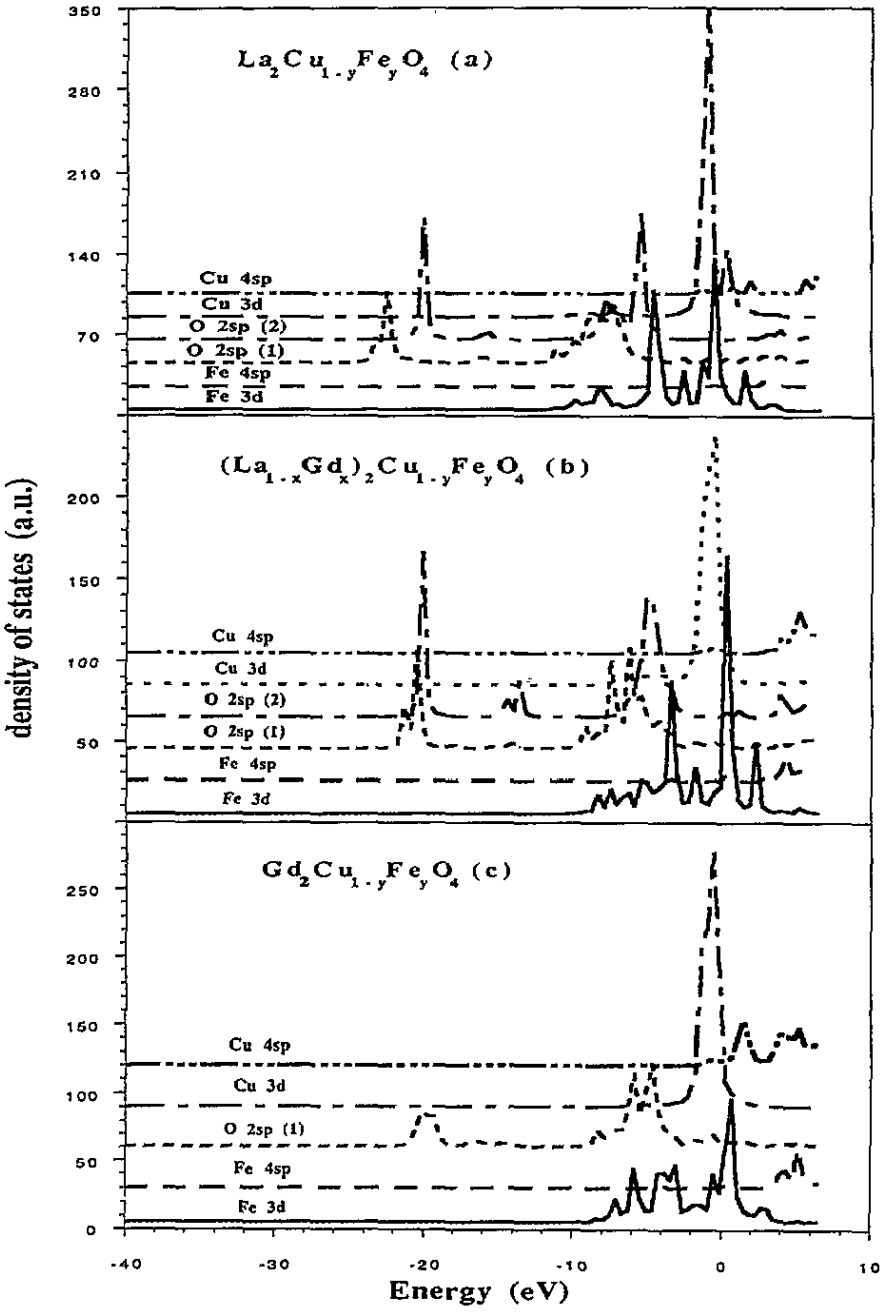

Figure 5. PDOS of (a) $La_2Cu_{1-y}Fe_yO_4$, (b) $(La_{1-x}Gd_x)_2Cu_{1-y}Fe_yO_4$, and (c) $Gd_2Cu_{1-y}Fe_yO_4$. Curves are offset vertically for energy viewing.

3.2.2. T phase.* The crystal structure for $(La_{1-x}Gd_x)_2CuO_4$ and $(La_{1-x}Gd_x)_2Cu_{1-y}Fe_yO_4$ was taken from the work of Gang Xiao *et al* on $(La_{1-x}Gd_x)_{1.85}$ $Sr_{0.15}CuO_4$ ($0.42 \leqslant x \leqslant 0.49$) [8]. As shown in table 2, the effective ionic configurations of centre Cu was found to be $Cu^{1.75+}3d^{9.15}4s^{0.07}4p^{0.02}$ with a very small antiferromagnetic (AF, with respect to Gd)

spin moment $-0.001\ \mu_B$. The oxygen effective charge in the centre plane (M–O bond length 1.92 Å) is about $-1.75e$, with a very small spin moment $0.004\ \mu_B$. On the axial site (M–O bond length 2.41 Å), the net oxygen charge is $-1.83e$ and the moment $0.003\ \mu_B$. The effective charges for La ions on four (a, b) plane sites and the top axial site are all about $+2.90e$, with a low, ferromagnetically coupled moment $\sim 0.0001\ \mu_B$. For Gd atoms on four (a, b) plane sites, the effective charge is about $+2.77e$, with a large moment $+6.91\ \mu_B$. We will see that this is very similar to the Gd configuration calculated for the Gd_2CuO_4 T′ structure.

Fe impurity calculations were carried out on the same cluster, with Fe substituted on the Cu(1) site. The resulting valence electron charge and spin populations are given in table 2. The effective charge of the centre-substituted Fe was found to be $+1.93e$, with a spin moment $3.92\ \mu_B$, AF coupled to Gd. We also found, in this case, that the spin moments for oxygen in the (a, b) plane and axial sites, and for La atoms both on four (a, b) and top axial sites, are greatly enhanced, with values 0.02, 0.02, 0.005, 0.006 μ_B, respectively, oriented parallel to Fe.

Valence charge density difference contour maps of $(La_{1-x}Gd_x)_2CuO_4$ and $(La_{1-x}Gd_x)_2Cu_{1-y}Fe_yO_4$ on (100) and (110) planes are shown in figure 6(a) and 6(b), respectively. On the (100) plane, we can see that the charge densities of the four equatorial oxygen atoms are noticeably increased after substituting Fe for Cu as in the T phase. The balance between four equatorial O(1) atoms and the O(3) atoms on upper or lower (a, b) plane sites has been altered, since the charge density contours are a little deformed toward O(3). The charge density around the axial O(2) atom is increased toward the centre site, but decreased toward the axial La(1) site. We have already noted that O(1) and O(2) leave very similar spectral distributions, see figures 4 and 5. On the (110) plane, the charge densities around the Gd and La(2) ions are all increased after Fe substitution. Referring to table 2, we find that both charges decrease $0.01e$ compared to the pure Cu case; i.e. become locally less ionic.

The PDOS for Cu(1) 3d, 4sp, O(1) and O(2) 2sp in $(La_{1-x}Gd_x)_2CuO_4$ are shown in figure 4(b), for Fe 3d, 4sp, Cu(2) 3d, 4sp, O(1) and O(2) 2sp in $(La_{1-x}Gd_x)_2Cu_{1-y}Fe_yO_4$ are shown in figure 5(b). Main features of T and T* phase DOS are very similar. The T* Cu 3d peak is relatively narrower, and the covalent Cu–O structure does not extend as far below E_F. The PDOS of the axial oxygen O(2) lies above that of centre plane O(1) atoms by 1 eV, again correlating with its increased bond length.

3.2.3. T′ phase. For Gd_2CuO_4, the effective configuration of Cu shown in table 3 was found to be $Cu^{1.57+}3d^{9.25}4s^{0.14}4p^{0.04}$; covalent charge sharing with oxygen in the (a, b) plane, leads to an effective charge of $1.57e$. The net Cu charges T (1.83) > T* (1.75) > T′ (1.57) thus correlate directly with the number of oxygen ligands. Spin on the copper ion at the centre is only about $-0.02\ \mu_B$ oriented in the opposite sense to the large Gd moment. Peripheral Cu_4, also in the (a, b) plane show a large AF-coupled moment of $-0.65\ \mu_B$. The Gd ions on the axial sites or on the (a, b) plane, are found to have an effective charge about $+2.70e$, a little less ionic than the normal trivalent state. The Gd moments, near the attainable maximum, are all parallel with magnitude about 6.80–6.90 μ_B.

Fe impurity calculations were carried out on the 27-atom cluster Fe–O(4)–Gd(8)–O(8)–Cu(4)–Gd(2) embedded in the previously obtained Gd_2CuO_4 self-consistent lattice, yielding a configuration of $Fe^{1.84+}3d^{6.01}4s^{0.11}4p^{0.04}$ with spin moment of $+3.82\ \mu_B$. Covalent interactions with oxygen add $0.11e$ and $0.04e$ to Fe 4s and 4p atomic orbital occupation. The fourfold equatorial oxygens exhibit ferromagnetic coupling to the central metal ion,

Table 3. Charge and spin atomic orbital population for T′ phase M–O(4)–Gd(8)–O(8)–Cu(4)–Gd(2) clusters.

		M = copper		M = iron	
		Charge	Spin	Charge	Spin
M[a]	3d	9.25	−0.019	6.01	3.791
	4s	0.14	−0.003	0.11	0.019
	4p	0.04	0.001	0.04	0.009
Total		1.57	−0.021	1.84	3.817
O[b]	2s	1.97	0.001	1.97	0.001
	2p	5.73	−0.013	5.76	0.100
Total		−1.70	−0.012	−1.73	0.101
Gd[c]	4f	7.20	6.770	7.20	6.772
	5p	5.97	0.007	5.97	0.010
	5d	0.10	0.024	0.10	0.022
	6s	0.03	0.001	0.03	−0.003
Total		2.70	6.802	2.70	6.802
Cu[d]	3d	9.15	−0.633	9.14	0.684
	4s	0.19	−0.014	0.19	0.022
	4p	0.03	−0.001	0.02	0.001
Total		1.63	−0.648	1.65	0.707
Gd[e]	4f	7.11	6.843	7.11	6.857
	5p	5.96	0.019	5.96	0.023
	5d	0.12	0.037	0.10	0.032
	6s	0.03	0.001	0.04	0.002
Total		2.78	6.900	2.80	6.914
O[f]	2s	2.00	−0.000	2.00	0.000
	2p	5.57	0.136	5.59	0.181
Total		−1.56	0.136	−1.59	0.182

[a] Cu(1) or Fe at the centre.
[b] O(1) on four (a, b) centre plane sites.
[c] Gd(1) on four (a, b) plane sites.
[d] Cu(2) on centre plane sites.
[e] Gd(2) axial sites.
[f] O(2) on four (a, b) lower plane sites.

with moment $+0.10\ \mu_B$, in marked contrast to their interaction with Cu.

Valence charge density difference contour maps of $Gd_2Cu_{1-y}Fe_yO_4$ versus Gd_2CuO_4 on the (100) and (110) planes are shown in figure 7(a) and (b), respectively. On the (100) plane, we can see that the equatorial O(1) charge densities and especially the bond region densities are increased after substituting Fe at the centre site. The bond length between oxygen and the centre site is about 1.95 Å, which is intermediate to the values for the T phase. The charge densities on the next-nearest Cu(2) sites are somewhat decreased compared to the pure Cu case.

The axial Gd(2) atoms have reduced interaction with the oxygen atoms O(2) in the upper and lower (a, b) planes. On the (110) plane, we can see the charge density differences around the Gd atoms much more clearly. After substituting Fe for Cu, the fourfold Gd(1) atoms show a small increase in charge densities, polarized toward the axial Gd(2), while the charge densities around the Gd(2) atoms decrease. Thus secondary-bonding interaction effects due to Fe extend outward to at least third neighbours.

The PDOS for Cu(1) 3d, 4sp and O(1) 2sp in Gd_2CuO_4 are shown in figure 4(c).

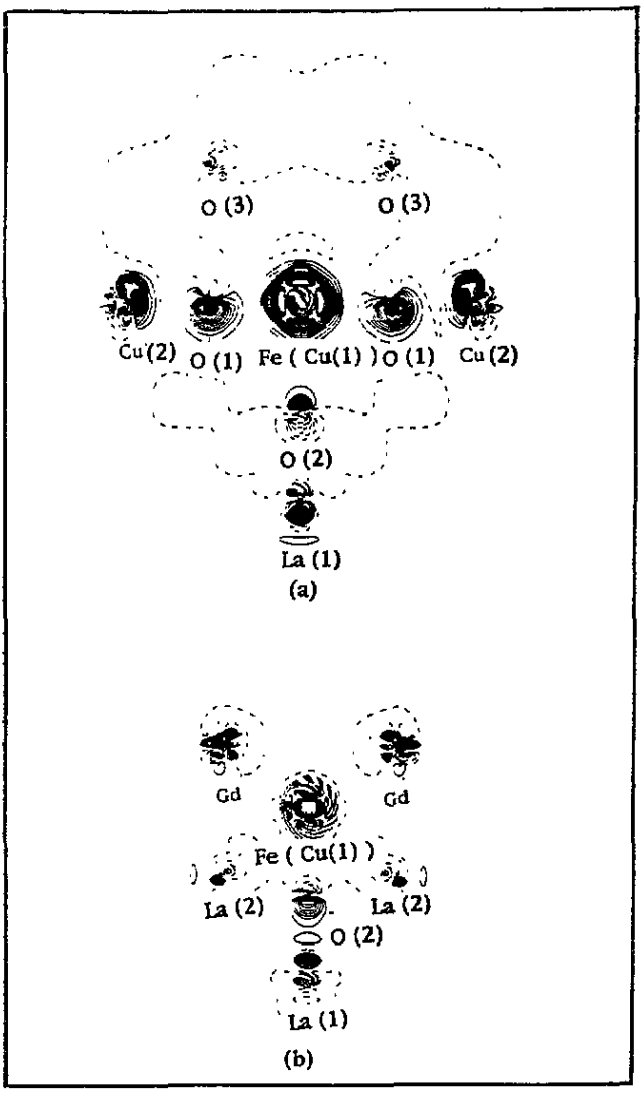

Figure 6. - - - Valence charge density difference contour map of T* phase: the difference $\rho[La_{1-x}Gd_x)_2Cu_{1-y}Fe_yO_4)] - \rho[(La_{1-x}Gd_x)_2CuO_4]$ on (a) (100) plane containing four equatorial oxygen, $-1.50 < \rho < 0.30e/a_0^3$; (b) (110) plane containing one axial oxygen, $-0.55 < \rho < 0.80e/a_0^3$. Contour interval is $0.01e/a_0^3$; dotted lines are negative values.

Corresponding Fe 3d, 4sp are shown in figure 5(c). As may be expected from the foregoing discussion, the fourfold-coordinated Cu d bond is further narrowed in comparison with T and T* phases, and the 'covalent tail' is further weakened. There is one major peak for the Fe 3d PDOS around the Fermi level and several smaller peaks 3–8 eV below the Fermi level. Unlike the T and T* phases the Fe 3d spectrum does not resolve itself into identifiable 'crystal field', exchange splitting, and Fe d/O p covalency features. Rather, they are overlapping and mixed here, forming a band extending to about 8 eV below E_F, appreciably less (~10–11 eV) than that of the fivefold- and sixfold-coordinated phases. A small charge transfer to the Cu 4s, 4p states is noted.

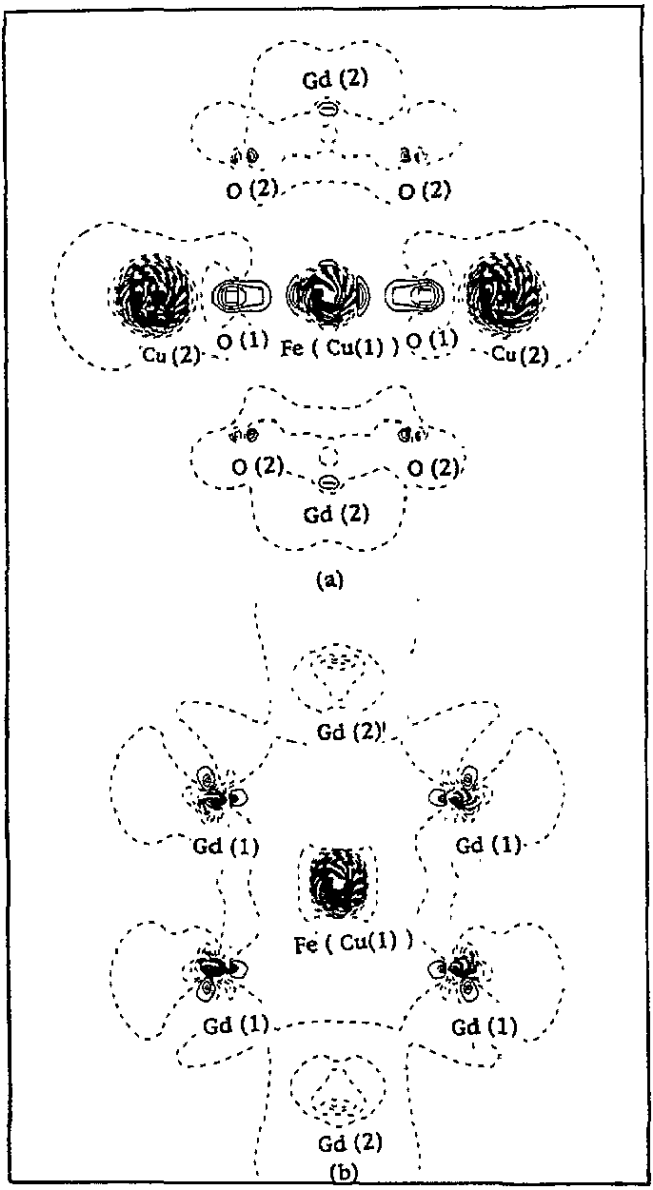

Figure 7. - - - Valence charge density difference contour map of T′ phase: $\rho[Gd_2Cu_{1-y}Fe_yO_4)] - \rho[Gd_2CuO_4]$ on (a) (100) plane containing four equatorial oxygen, $-3.40 < \rho < 0.04e/a_0^3$; (b) (110) plane, $-3.30 < \rho < 0.05e/a_0^3$. Contour interval is $0.01e/a_0^3$; dotted lines are negative values.

3.3. Hyperfine interactions

Theoretical and experimental Mössbauer spectroscopy studies have been made concerning the hyperfine structures in iron-substituted superconducting oxides [4–7]. In order to give an accurate description of $\rho_c(0)$ and $\rho_s(0)$, core polarization/relaxation effects have to be considered. In the present work, core contributions were determined by separate numerical atomic calculations using the self-consistent atomic configurations. In this way basis set

truncation limitations were entirely avoided. The charge densities obtained here provide a means for interpreting the IS of the three compounds, which we wish to relate to coordination and bond length.

The calculated EFG tensors for iron in T, T* and T′ phases are listed in table 4.

Table 4. Hyperfine parameters for substitutional Fe impurity in T, T*, and T′ phases. Values are given for valence electron matrix elements $V_{aa}^{\text{valence}} = \rho_c(3x_a^2 - r^2)/r^5$. The total EFG required to determine the quadrupole splitting is found by combining contributions of exterior crystal ions, core electrons, and nuclei of the local cluster with the appropriate sign, as discussed in text.

	T phase	T* phase	T′ phase[a]
Charge density $\rho_c(0)$ (e/a_0^3)			
Valence	4.24	4.01	3.97, 3.88
Core	11 868.97	11 869.00	11 870.18, 11 870.92
Spin density $\rho_s(0)$ (e/a_0^3)			
Valence	0.65	0.47	0.31, 0.44
Core	−1.10	−1.09	−1.31, −1.10
Total	−0.45	−0.62	−1.00, −0.66
Fe 3d moment (μ_B)	4.02	3.91	3.79, 3.95
EFG tensor (e/a_0^3)			
$V_{xx} = V_{yy}$	−0.49	−0.38	−0.53, 0.52
V_{zz}	1.00	0.76	1.07, 1.02

[a] In T′ phase, values are given for simple fourfold substitution, and for a fivefold site with additional O at axial position as in T*.

In table 5, calculated and experimental results are presented for isomer shift, quadrupole splitting, and magnetic hyperfine field for Fe impurity clusters representing T, T* and T′ phases. The experimental data refer to specimens containing 7% Sr substituted for La, i.e. $(La_{1-x}Gd_x)_{1.85}Sr_{0.15}(Cu_{1-y}Fe_y)O_4$. Measurements have been made over the range of iron concentration $y = 0.005$ to 0.05; the $y = 0.01$ data are discussed here. According to our present understanding, we may distinguish five different spectra corresponding to five different hypothetical Fe environments generated in the T → T* → T′ phases encountered under Gd substitution for La. In the $0 \leqslant x \leqslant 0.4$ range one finds

(A) the 'ideal' T phase distorted octahedral sixfold site, and
(B) a site associated with oxygen interstitials.

In the $0.4 \leqslant x \leqslant 0.8$ range one finds spectra B and

(C) associated with the 'ideal' T* fivefold pyramidal site.

For complete Gd substitution, $x = 1$, we observe spectra C, and

(D) associated with an oxygen interstitial, fivefold distorted pyramidal, and
(E) the 'ideal' T′ phase fourfold site.

The assignment of spectra A–E to specific site geometry and oxygen coordination is consistent with the observed amplitude dependence upon oxygen content, and the known propensity of iron to accumulate oxygen in its coordination region.

Table 5. Calculated and experimental isomer shift (mm s^{-1}), quadrupole splitting (mm s^{-1}), and magnetic hyperfine contact field (T) for Fe substitution on Cu site in T, T* and T′ phases.

	T phase		T* phase		T′ phase		
	A	B	B	C	C	D	E
IS experiment[a]	0.00	−0.02	0.00	0.02	0.04	−0.38	−0.13
Theory[b]	0.00			0.05		−0.40	−0.23
QS experiment[c]	1.69	1.46	1.04	0.73	0.60	0.68	1.62
Theory[d]	0.94			0.72		0.96	1.01
H_s experiment[e]	±41		±46	±43		—	
Theory[f]	−23.5			−32.4		−34.5	−52.2

[a] Experimental results for T, T* and T′ systems with respect to T phase; with reference to α-Fe, IS(T phase) = 0.27 mm s^{-1} [27]. The measurements were made on Sr-doped compounds as follows: T phase: $La_{1.85}Sr_{0.15}(Cu_{1-x}Fe_x)O_4$; T* phase: $(La_{0.55}Gd_{0.45})_{1.85}Sr_{0.15}(Cu_{1-x}Fe_x)O_4$; T′ phase: $Gd_{1.85}Sr_{0.15}(Cu_{1-x}Fe_x)O_4$, with $x = 0.01$. Species A, B, C, D, E are discussed in text.

[b] Calculated results with reference to T phase using $IS = A_{IS}\,\Delta\rho_c(0)$, $A_{IS} = -0.25$ mm a_0^3 s^{-1}.

[c] Experimental data [27].

[d] Calculated with $B = 11.77$ mm a_0^3 b $^{-1}$ s^{-1}, $Q = 0.08$ b, see (6).

[e] Experimental [28], 3% Fe/Cu substitution, at 4.2 K.

[f] $A_s = 52.42$ T a_0^3, see (9).

One aim of the present cluster calculations is to verify whether these assignments are compatible with theoretical electronic structures. In order to minimize systematic errors due to basis set incompleteness, cluster size effects, relativistic effects, and intrinsic errors of density functional theory, table 5 shows the calculated IS results with respect to a reference state $La_2Cu_{1-y}Fe_yO_4$, $y \to 0$ using equation (5) with $A_{IS} = -0.25$ mm a_0^3 s^{-1}. For the T′ phase we considered fourfold substitutional Fe (−0.23 mm s^{-1}) and Fe in fivefold coordination (−0.40 mm s^{-1}) similar to that found in the T* phase. The results are reasonably close to the experimental data, noting again the essential Sr content (due to lattice stability requirements) of the specimens.

We further considered some effects of local lattice relaxation on the sixfold, fivefold, and fourfold Fe–O bond lengths in T, T*, and T′ phases respectively. The calculation results show that the IS increases in each phase as the bonds shorten at the rate $\delta IS/(\delta R/R) \cong$ T (−2.0) < T*(−2.2) < T′(−5.2) mm s^{-1}. Concerning the T′ phase, we see that a 3% bond contraction of the relatively open fourfold coordination could reproduce the experimental value at −0.38 mm s^{-1}. However, that would leave unexplained the −0.23 mm s^{-1} value which we have assigned as the unrelaxed fourfold site. A more natural explanation, which also fits the data, is that Fe has sometimes accumulated an extra apical oxygen (−0.40 mm s^{-1}) essentially identical to that found in T*. In any case, our results demonstrate that the IS is a sensitive function of the Fe–O bond length and coordination.

Using (6) and (7) with $Q(^{57}Fe) = 0.08$ b and the data in table 4, we find $QS(^{57}Fe) =$ 0.94 mm s^{-1}, 0.72 mm s^{-1}, and (1.01, 0.96) mm s^{-1}, for T, T*, and T′ phases respectively. The experimental data for QS in the three phases are reported in [27]; several distinct spectra are observed. In the T phase, QS of about 1.69 mm s^{-1} and 1.46 mm s^{-1}, in the T* phase, 1.04 mm s^{-1} and 0.73 mm s^{-1}, and in the T′ phase, QS = 0.60 mm s^{-1}, 0.68 mm s^{-1}, and 1.62 mm s^{-1}. The ^{57}Fe nuclear quadrupole moment Q is generally estimated to be in the range 0.08 b–0.21 b, with the smaller values preferred. Thus we use the value $Q = 0.08$ b in the data presented in table 4, for unrelaxed lattice sites, and in the case of T′, an additional

fivefold site with interstitial oxygen. The multiplicity of experimental data makes unique definition of sites difficult. We see that measured T phase values are 55 and 80% larger than calculated values; this could suggest a larger value of Q, or a locally relaxed lattice geometry. The calculated sensitivity of QS to local Fe–O bond contraction is rather large: $\delta QS/(\delta R/R) \cong 1.0$ mm s^{-1} for T and T′ phases, and 5.5 mm s^{-1} for T* phase. However, a 6% bond contraction in sixfold coordination only raises QS to 1.0 mm s^{-1}. We suggest that a value of $Q \cong 0.13$–0.14 b would be generally more consistent with experiment.

The calculated Fe magnetic hyperfine fields $H_s(0)$ are -23.5 T for T phase, -32.4 T for T* phase, and $(-52.2, -34.5)$ T for T′ phase. Experimental absolute values for spectra B and C are 46 T and 43 T respectively; while even at a temperature of 4.2 K no clear magnetic hyperfine pattern is found in the T′ phase, only a rather broad line indicating the presence of relaxation effects [28]. This can be rationalized in terms of fast Fe spin fluctuations, permitted by the weaker coupling to neighbouring Cu of fourfold-coordinated Fe. Applied field measurements are being undertaken to resolve this point.

The Fe magnetic hyperfine field is dominated here by the negative core polarization contribution. For a fixed 4sp population the core field will be proportional to the driving 3d electron moment; the proportionality of the moment and $H_s(0)$ is often assumed in analyses of experimental data. However, with variation of the diffuse 4sp occupancy due to interactions with ligands, this proportionality is lost, as can be seen in table 4. The sizable positive 4s contributions to $H_s(0)$ have to be invoked to explain properties of iron alloys and metallic impurity systems. Only the electronic spin contact contribution is considered here and no attempt has been made to include orbital and dipolar contributions from other crystal sites, as they are considered to be relatively small. The calculated Hs are in only fair agreement with experiment; the most obvious defect being the too-weak predicted field for the octahedral T phase site, which is correlated with the too-small Cu moments also calculated. In view of the sensitivity of H_s to the diffuse 4s contributions just discussed, it seems that further magnetic studies should be carried out in the context of larger cluster models.

4. Conclusions

We have reported theoretical calculations of electronic structure and hyperfine interactions of iron substituted for copper in T, T*, and T′ phases of $(La_{1-x}Gd_x)_2CuO_4$, using an embedded cluster model. The local density results have been discussed in the light of Mössbauer measurements and structure data for sixfold (T), fivefold (T*) and fourfold (T′) oxygen coordinations to Cu and Fe. We find that while formally divalent, the net charge on Cu diminishes with reduced oxygen coordination T > T* > T′: $1.83 > 1.75 > 1.57e$. This reflects the reduced ionic binding capacity of 6−, 5−, and 4− ligands, and appears primarily as an increase in the Cu 3d population. The predicted net Cu spin, induced by the large but distant Gd moment, remains very small, attaining $-0.02\ \mu_B$ in T′. This is one order of magnitude smaller than experimental values. Iron substituting for Cu is also formally divalent, with calculated net charge trend T > T* > T′: $2.06 > 1.93 > 1.84e$ similar to Cu. A high Fe spin moment associated with the d6 occupancy is found, with values T > T* > T′: $4.13 > 3.91 > 3.82\ \mu_B$, which are consistent with large experimental $H_s(0)$ values.

The experimental IS falls generally within the range normally associated with the d^5 configuration of trivalent iron [29], with one exception, the line 'D' of the T′ phase. Our calculated 3d populations (e.g. $3d^{5.85}$ in unrelaxed T phase) include both an ionic 'crystal field' component and a contribution arising from Fe–O covalency. In strongly covalent

oxides, the latter contribution can amount to 0.5–1.0*e* [30], thus accounting for the apparent discrepancy between the experimental assignment of ionic state and calculated charges. On the other hand, the $Sr^{2+} \rightarrow La^{3+}$ substitution in the real materials creates a change imbalance which has to be compensated by the lattice. It is possible that iron located near Sr sites may adopt the Fe^{3+} state, and further calculations to explore this possibility would be interesting. Work in progress seeks to determine electronic structure associated with divalent dopants [31].

Hyperfine properties (IS, QS, H_s) associated with the Fe-substituted Cu site show trends similar to experiment, but interpretation is complicated by the presence of multiple sites in each phase. We have considered a local lattice relaxation model with six-, five- and fourfold oxygen atom contraction around the centre iron, to demonstrate the high IS sensitivity to bond length. The second, larger IS (-0.38 mm s^{-1}) seen experimentally in the T′ phase is strong evidence for an Fe site which has accumulated an additional oxygen ligand. The calculated IS $= -0.40$ mm s^{-1} is close to experiment, while the calculated QS $= 0.96$ mm s^{-1} is larger than experiment (0.75 mm s^{-1}). We have already noted that QS calculated for T and T* phases are about $\frac{2}{3}$ of experiment at values, perhaps due to the choice of $Q \cong 0.08$ b. However, lattice distortion is also indicated as important in T′, since the theoretical QS for the fourfold site is too large. We suggest that energy minimization studies of local relaxation will be needed to resolve further details of the local geometry. The predicted large moment and 52 T contact field in the fourfold T′ site await experimental confirmation.

Acknowledgments

This work was supported by the US Department of Energy under grant No DE-FG02-84ER45097, by NSF-INT-9202608, and by CNPq, Brazil under grant No 910250-90-1.

References

[1] Bednorz J G and Müller K A 1986 *Z. Phys.* B **64** 198
[2] Jorgensen J D, Dabrowski B, Pei Shiyou, Hinks D G and Soderholm L 1988 *Phys. Rev.* B **38** 11 337
[3] Tokura Y, Takagi H and Uchida S 1989 *Nature* **337** 345
[4] Taniwaki M, Nakaya S and Muraki T 1993 *Nucl. Instrum. Methods Phys. Res.* B **76** 345
[5] Dunlap B D, Jorgensen J D, Kwok W K, Kimball C W, Matykiewicz J L, Lee H and Segre C U 1988 *Physica* C **153–155** 1100
[6] Ellis D E, Baggio-Saitovitch E and Lam D J 1992 *Physica* C **198** 57
[7] Ellis D E, Dunlap B D, Baggio-Saitovitch E, Souza Azevedo I, Scorzelli R B and Kimball C W 1988 *Applications of the Mössbauer Effect* ed E Baggio-Saitovitch, E Galvão da Silva and H R Rechenberg (Singapore: World Scientific)
[8] Xiao Gang, Cieplak M Z and Chien C L *1989 Phys. Rev. B* **40** *4538*
[9] Tamaki T, Komai T, Ito A, Maeno Y and Fugita T 1988 *Solid State Commun.* **65** 43
[10] Nowik I, Kowitt M, Feluer I and Bauminger E R 1988 *Phys. Rev.* B **38** 6677
[11] Sedykh V, Nasu S and Fujita F E 1988 *Solid State Commun.* **67** 1063
[12] Tang H, Qui Z Q, Du Y-W, Xiao Gang, Chein C L and Walker J C 1987 *Phys. Rev.* B **36** 309
[13] Kimball C W, Matykiewicz J L, Giapintzakis J, Dwight A E, Brodsky M B, Slaski M, Dunlap B D and Fradin F Y 1987 *Physica* B **148** 309
[14] Baerends E J, Ellis D E and Ros P 1973 *Chem. Phys.* **2** 40
[15] Rosen A, Ellis D E, Adachi H and Averill F W 1976 *J. Chem. Phys.* **65** 3629
[16] Ellis D E, Benesh G A and Byrom E 1979 *Phys. Rev.* B 20 1198
[17] Delley B and Ellis D E 1982 *J. Chem. Phys.* **76** 1949
[18] Ellis D E, Benesh G A and Byrom E 1977 *Phys. Rev.* B **16** 3308
[19] Ellis D E, Guo J and Lam D J 1991 *Rev. Solid State Sci.* **5** p 287
[20] Mulliken R S 1955 *J. Chem. Phys.* **23** 1833
[21] Shenoy G K and Wagner F E (ed) 1978 *Mössbauer Isomer Shifts* (Amsterdam: North-Holland)

[22] Guetlich P, Link R and Trautwein E A 1978 *Mössbauer Spectroscopy and Transition Metal Chemistry* (Berlin: Springer)
[23] Yang B X, Mitsuda S, Shirane G, Yamaguchi Y and Syono Y 1987 *J. Phys. Soc. Japan* **56** 2283
[24] Vaknin D, Sinha S K, Moncton D E, Johnston D C, Newsam J M, Safinya C R and King H E Jr 1987 *Phys. Rev. Lett.* **58** 2802
Uemura Y J, Kossler W J, Yu X H, Kempton J R, Schone H E, Opie D, Stronach C E, Johnston D C, Alvarez M S and Goshorn D P 1987 *Phys. Rev. Lett.* **59** 1045
[25] Yamaguchi Y, Yamauchi H, Ohashi M, Yamamoto H, Shimoda N, Kikuchi M, and Syono Y 1987 *Japan. J. Appl. Phys.* **26** L447
[26] Matykiewicz J M, Kimball C W, Giapintzakis J, Dwight A E, Brodsky M B, Slaski M, Dunlap B D and Fradin F Y 1987 *Phys. Lett.* **124A** 453
[27] Baggio-Saitovitch E, Marquez Jacom M A, Sanchez D R and Garcia S G 1994 *Physica* C **235–240** 865
Candela D R S 1994 *PhD Thesis* Centro Brasileiro de Pesquisas Fisicas
[28] Sanchez D R, Baggio-Saitovitch E and Litterst F J 1994 *Latin Am. Conf. on Applications of the Mössbauer Effect (LACME) (Santiago, Chile 1994)*
Sanchez D R, Baggio-Saitovitch E, Elmassalami M and Litterst F J 1994 *Latin Am. Conf. on Applications of the Mössbauer Effect (LACME) (Santiago, Chile 1994)*
[29] Ingalls R, Van Der Woude F and Sawatzky G A 1978 *Mössbauer Isomer Shifts* (Amsterdam: North-Holland)
[30] Press M R and Ellis D E 1987 *Phys. Rev.* B **35** 4438
[31] Wu Y, Ellis D E, Mason T O and Shen L unpublished